

Chapter 6

Astrometric Precision with MeerKAT

6.1 Introduction

Section 2.3.1 introduced several fundamental angular scales, one of which was the angular resolution,

$$\Theta_{\text{PSF}} \sim \frac{\lambda}{d_{\text{max}}}.$$

Quantified by the FWHM (Θ_{PSF}) of the PSF¹, the angular resolution is related to the observing wavelength (λ) and the maximum baseline length (d_{max}). While a reasonable first-order approximation, this equation assumes a circular Gaussian PSF and, thus, rotational symmetric sampling of the uv -plane. Complex array configurations or non-Zenith observations can cause the projected baseline vectors to be “squished” along one direction, resulting in elliptical Gaussian PSFs. By default, imaging software records the PSF parameters with the FWHM of the major axis (Θ_{maj}), the FWHM of the minor axis (Θ_{min}), and the beam position angle (θ_{bpa}) measured East

¹Here, we are referencing the idealized PSF, free from finite-sampling effects.

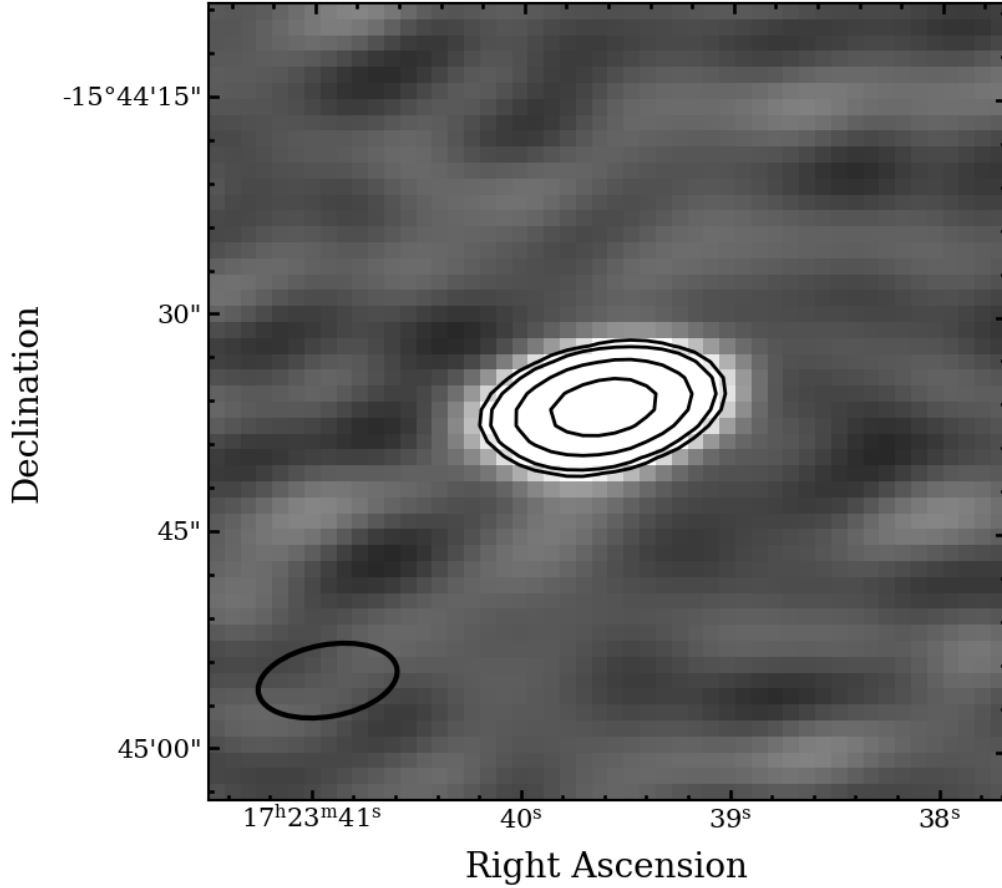


Figure 6.1: Example of a highly elliptical PSF (hollow black ellipse) and its effect on the shape of a point source. In this example, the source was observed at a shallow elevation of $\sim 30^\circ$ and an azimuth angle of $\sim 90^\circ$. The low elevation causes ellipticity, and the azimuth angle rotates the PSF to (roughly) align its major axis with the right ascension direction.

of North. Given that the PSF is an elliptical Gaussian, the PSF axes can be alternatively expressed as standard deviations, σ_{maj} and σ_{min} , recalling that $\text{FWHM} = \sqrt{8 \ln 2} \sigma$. The PSF is an instrument's point source response, so the ellipticity manifests as the shape of point sources (e.g., Figure 6.1).

The position of a point source is given by the centre of its (PSF-shaped) intensity distribution. Adopting the location of the peak pixel can provide a crude position approximation. However, the peak pixel is affected by pixelization errors if the *actual* peak is situated at a pixel boundary. Pixelization errors can be mitigated by decreasing the pixel size, although

this approach is prohibitively computationally expensive for interferometers with large fields of view. As a result, the positions of point sources are measured by fitting Gaussian components to their intensity distributions, the approach adopted in the previous chapters. Assuming the pixel size adequately samples the PSF (i.e., $\Theta_{\min} \sim 3\text{--}5$ pixels), Gaussian fitting also mitigates pixelization.

Kaper et al. (1966) derived analytic equations for the key parameters and their errors (peak amplitude, central position, and width) measured from one-dimensional Gaussian fitting, assuming uncorrelated Gaussian noise in each pixel. Later, Condon (1997, CR97) derived analytic solutions for two-dimensional data with uncorrelated noise and semi-analytic equations for spatially correlated noise (see also, Condon et al., 1998); the latter applies to synthesis imaging as the PSF acts as a smoothing kernel correlating adjacent pixels. CR97 showed that the variance in the position,

$$\sigma_k^2 \sim \left(\frac{\mathcal{D}_k}{S/N} \right)^2, \quad (6.1)$$

is a function of the signal-to-noise ratio and the *extent* of the Gaussian (\mathcal{D}_k) along direction k (where k is RA or Dec). The extent is a function of the PSF shape, $\mathcal{D}_k = \mathcal{D}_k(\Theta_{\text{maj}}, \Theta_{\text{min}}, \theta_{\text{pa}})$, where elliptical PSFs have $\mathcal{D}_{\text{RA}} \neq \mathcal{D}_{\text{Dec}}$ (see Equation 21 and 41 in CR97). For a circular PSF ($\Theta_{\text{maj}} \equiv \Theta_{\text{min}}$), Equation (6.1) simplifies to,

$$\sigma_k = \frac{\Theta_{\text{maj}}}{\sqrt{8 \ln 2} (S/N)} = \frac{\sigma_{\text{maj}}}{S/N}. \quad (6.2)$$

Some source-finding software packages, like PYBDSF, adopt the CR97 equations to quantify astrometric errors. However, in CR97, the variance was assumed to originate from Gaussian noise, ignoring the effects of sparse uv -sampling or incomplete deconvolution of extended sources, where artefacts produce large-scale non-Gaussian “noise”. Moreover, Equations (6.1) and

(6.2) neglect the potential for signal-to-noise independent systematics from, for example, calibration errors. As a result, many radio astronomers adopt a heuristic astrometric error of the form,

$$\sigma_k \sim \mathcal{D}_k \sqrt{\left(\frac{A}{S/N}\right)^2 + B^2}. \quad (6.3)$$

Consistent with CR97, Equation (6.3) is proportional to the PSF size, scaling inversely with the fitted component's signal-to-noise ratio while now including a systematic *floor* on the astrometric error. The next question: what are the correct choices for \mathcal{D}_k , A , and B ?

Recommendations for A and \mathcal{D}_k can vary depending on whose asked and without clear justification. For \mathcal{D}_k , a common, conservative assumption is $\mathcal{D}_{\text{RA}} \equiv \mathcal{D}_{\text{Dec}} \equiv \Theta_{\text{maj}}$. Alternatively, the ellipticity is typically accounted for by using the size of the rectangle bounding the PSF,

$$\mathcal{D}_{\text{RA}} = \sqrt{(\Theta_{\text{maj}} \sin \theta_{\text{bpa}})^2 + (\Theta_{\text{min}} \cos \theta_{\text{bpa}})^2}, \quad (6.4)$$

$$\mathcal{D}_{\text{Dec}} = \sqrt{(\Theta_{\text{maj}} \cos \theta_{\text{bpa}})^2 + (\Theta_{\text{min}} \sin \theta_{\text{bpa}})^2}, \quad (6.5)$$

or the lengths from the centre to the ‘edge’ of the PSF,

$$\mathcal{D}_{\text{RA}} = \frac{\sigma_{\text{maj}} \sigma_{\text{min}}}{\sqrt{(\sigma_{\text{maj}} \sin \theta_{\text{bpa}})^2 + (\sigma_{\text{min}} \cos \theta_{\text{bpa}})^2}}, \quad (6.6)$$

$$\mathcal{D}_{\text{Dec}} = \frac{\sigma_{\text{maj}} \sigma_{\text{min}}}{\sqrt{(\sigma_{\text{maj}} \cos \theta_{\text{bpa}})^2 + (\sigma_{\text{min}} \sin \theta_{\text{bpa}})^2}}. \quad (6.7)$$

For A , the most common values are $A = 1$ and $A = 1/2$, where the latter likely originates from the fact that $1/\sqrt{8 \log 2} \approx 1/2.355 \sim 1/2$. To remain approximately consistent with CR97, $A = 1$ **should** be chosen if using *radial* \mathcal{D}_k values (e.g., Equation 6.6 & 6.7) and $A = 1/2$ if using *diameter-like* \mathcal{D}_k values (e.g., Equation 6.4 & 6.5). Incorrect pairings can overestimate errors,

potentially missing results, or underestimate errors, artificially increasing the significance of any astrometry-driven phenomenon.

The systematic limit, B , does not have the same theoretical motivation as A and thus can vary significantly from instrument to instrument. The VLA, possibly the best-known interferometer, recommends a systematic error of $\sim 10\%$ the PSF FWHM². Newer facilities, like MeerKAT, do not have similar recommendations, leading a widespread *ad hoc* adoption of the $\sim 10\%$ VLA systematic. Investigating what systematic limit is appropriate for MeerKAT was the initial motivation for this research.

A last, often overlooked effect is the correlated RA and Dec errors resulting from PSFs with misaligned principle axes (i.e., $\theta_{\text{pa}} \neq 0, \pi/2, \pi \dots$). Consider an elliptical PSF with $\theta_{\text{pa}} = \pi/4$; a same-sign deviation (e.g., towards North-East) in RA and Dec is more likely than an opposite-sign deviation (e.g., towards North-West) of equal magnitude. Framing this effect probabilistically, when sampling from a two-dimensional Gaussian, for a fixed radial separation ($r = \sqrt{x^2 + y^2}$), stochastic deviations along the beam position angle are the most likely to occur. While CR97 appropriately treated the co-variances, the heuristic forms of \mathcal{D}_k given by Equations (6.4), (6.5), (6.6), & (6.7) will not enclose the same confidence region for all elliptical PSFs.

This chapter defines a simple yet powerful method to measure astrometric error. Wide-field interferometers like MeerKAT detect thousands of background or foreground point sources in a single observation. The variations in the positions observed during time-domain monitoring of a single pointing (i.e., *field*) will sample from the underlying astrometric error distribution, allowing for its empirical determination.

²<https://science.nrao.edu/facilities/vla/docs/manuals/oss/performance/positional-accuracy>

6.2 Methods

Section 3.6.1 presented an early version of this routine, originally designed to understand the astrometric variability of SAX J1810. Here, we assume the astrometric error adopts a similar functional form as the published version,

$$\hat{\sigma}_r = \sqrt{\left(\frac{A}{S/N}\right)^2 + B^2}. \quad (6.8)$$

The fundamental assumption (based on CR97) is that the astrometric error is proportional to some angular scale $\mathcal{D}_r(\Theta_{\text{maj}}, \Theta_{\text{min}}, \theta_{\text{pa}})$. To account for variable PSFs, we solve for a dimensionless ‘relative astrometric error’ $\hat{\sigma}_r = \sigma_r/\mathcal{D}_r$; where $\hat{\sigma}_r$ is the astrometric error measured in units of ‘PSFs’, and can be converted to physical units given that \mathcal{D}_r is always known. In contrast with the published version, we account for correlated errors by solving for total angular offsets rather than decomposing the offsets into RA and Dec components (hence the change from index \mathcal{D}_k to \mathcal{D}_r).

6.2.1 Offset Geometry

A schematic of the offset geometry is shown in Fig. 6.2. For a single measurement of a point source, stochastic variability offsets the measured position (α, δ) from its true position (α_0, δ_0) by some angular distance r and an offset direction defined by the *offset position angle* (ϕ_{pa}) measured East of North. Similar to the dimensionless astrometric error, the dimensionless separation, $\hat{r} = r/\mathcal{D}_r$, is normalized by the distance from (α, δ) to the elliptical confidence region described by the PSF-shape (shown as a black ellipse in Fig. 6.2)

For an elliptical Gaussian with variances of σ_{maj}^2 and σ_{min}^2 , and no

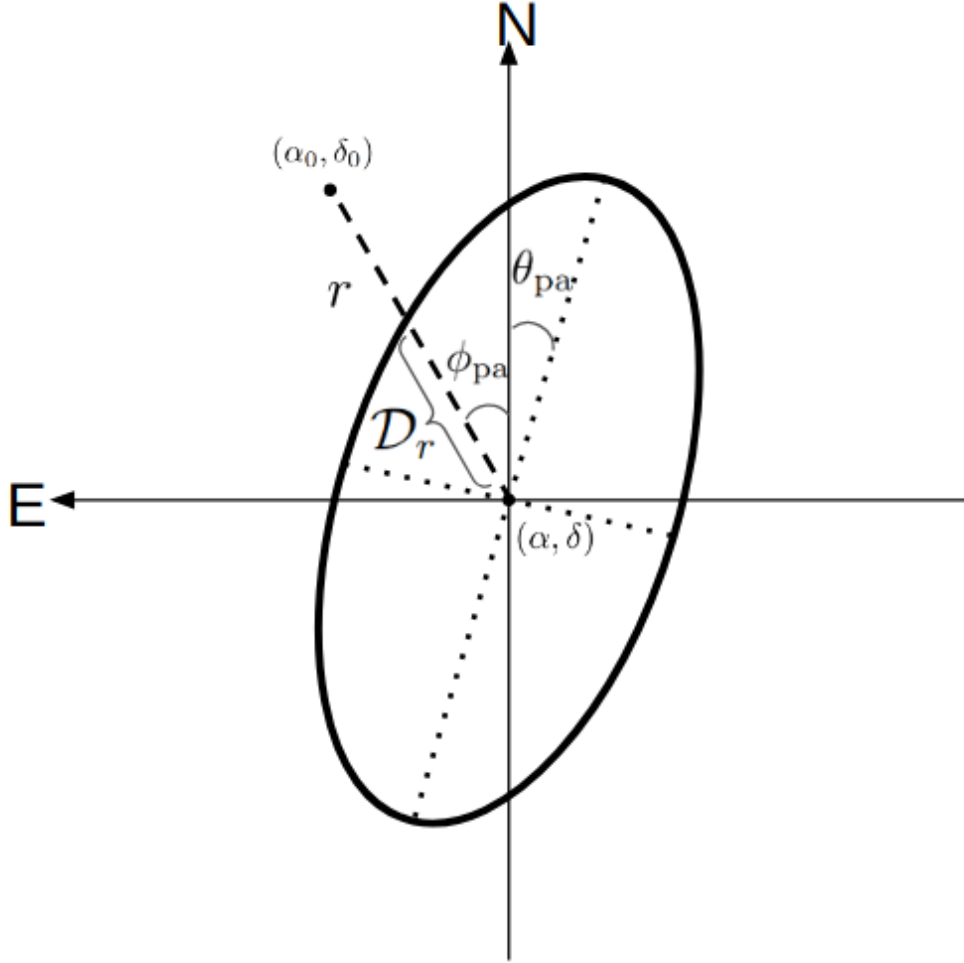


Figure 6.2: Schematic representation of the offset geometry. The measured position, (α, δ) , is offset from the true position, (α_0, δ_0) , by an angular separation \hat{r} . The r is rotated East of North by the offset position angle ϕ_{pa} . \mathcal{D}_r is the distance from (α, δ) to the elliptical confidence region defined by the PSF. The position angle of the elliptical confidence is given by θ_{pa} , but the major and minor axis (represented by the dotted lines) are dependent on the confidence interval of interest (e.g., 68%, 95%, 99.7%, ...)

covariance, an arbitrary confidence region is described by,

$$s = \left(\frac{\Delta_{\text{maj}}}{\sigma_{\text{maj}}} \right)^2 + \left(\frac{\Delta_{\text{min}}}{\sigma_{\text{min}}} \right)^2. \quad (6.9)$$

here, Δ_{maj} and Δ_{min} are the zero-point offsets along the major and minor axes, and s depends on the confidence region of interest. Equation (6.9) is the sum of squares of independent normally distributed variables, and thus s follows the χ^2_ν -distribution for two degrees of freedom ($\nu = 2$),

$$P(\chi^2_{\nu=2} \leq s) = P_0, \quad (6.10)$$

for a confidence region probability, P_0 . We choose $P_0 = 0.68$ (1σ), and thus $s \approx 2.279$. However, the choice is arbitrary, and different P_0 values will scale A and B appropriately, as long as P_0 remains consistent for observations with different PSF shapes. The confidence region is an ellipse with major and minor axes equal to $\sqrt{s}\sigma_{\text{maj/min}}$. Recognizing that the line connecting (α_0, δ_0) and (α, δ) passes through the ellipse at an angle of $\xi = \phi_{\text{pa}} - \theta_{\text{pa}}$,

$$\Delta_{\text{min}} = \Delta_{\text{maj}} \tan \xi \quad (6.11)$$

and Equation (6.8) becomes,

$$\Delta_{\text{maj}} = \frac{s\sigma_{\text{maj}}\sigma_{\text{min}}}{\sigma_{\text{maj}} + \sigma_{\text{min}} \tan \xi}, \quad (6.12)$$

where \mathcal{D}_r is,

$$\mathcal{D}_r = \sqrt{\Delta_{\text{maj}}^2 + \Delta_{\text{min}}^2}. \quad (6.13)$$

Knowledge of the measured position, true position, and PSF properties is sufficient to solve for r , \mathcal{D}_r , and thus, \hat{r} . As \hat{r} is positive definite, repeated observations of an arbitrary source j will sample a Rayleighian distribution

with a scale factor equivalent to the dimensionless astrometric error, $(\hat{\sigma}_r)_j$. For a source observed over N epochs, we can estimate its astrometric error from the sample distribution (Siddiqui, 1964),

$$(\hat{\sigma}_r)_j \approx \frac{\Gamma(N)\sqrt{N}}{\Gamma(N + \frac{1}{2})} \sqrt{\frac{1}{2N} \sum_{i=1}^N \hat{r}_{i,j}^2}. \quad (6.14)$$

Monitoring several sources at different signal-to-noise ratios is sufficient to derive A and B from Equation (6.8).

6.2.2 Workflow

The following routine utilizes the positional variability of field sources to determine an astrometric error in time-domain observations. Assuming a single image has been made for each observation, we use PYBDSF to make per-observation source catalogues. PYBDSF models the sky intensity distribution as a collection of Gaussian *components*. Components are then grouped into *sources* based on their relative separations and intensities³. The sources are then associated with *islands* — contiguous regions of pixels with values greater than some threshold value (`thresh_isl` in PYBDSF), and at least one pixel greater than the source detection threshold (`thresh_pix` in PYBDSF); both thresholds are expressed in units of rms deviations from the mean background intensity. We chose values of `thresh_isl=3` and `thresh_pix=4`.

The PYBDSF source catalogues include the peak intensity (F_p), the island flux density (F_i), and the source sizes quantified by major (Θ_M) and minor (Θ_m) axes. PYBDSF also classified each source as S- (single-component source, single-source island), C- (single-component source, multi-source island), or M-type (multi-component source).

We are interested in the astrometric error for the point source fitting.

³see <https://pybdsf.readthedocs.io/en/latest/algorithms.html> for more information

Thus, we remove resolved sources from the catalogues. To make it easier to identify point sources, the shapes of all Gaussian components are fixed to that of the PSF (`fix_to_beam=True` in PYBDSF), and components within an island are grouped into a single source (`group_by_isl=True` in PYBDSF). These flags make the classification binary, with S-types and (C or M)-types corresponding to point sources and resolved sources, respectively. By definition, all S-type sources will follow the strict definition of a point source; $F_i \sim F_p$ and $\Theta_{M/m} \equiv \Theta_{\text{maj/min}}$. However, noise fluctuations or imaging artefacts can cause PYBDSF to fit additional sub-dominant components, causing some point sources to be misclassified as resolved. To avoid excess source removal, we adopt an empirically motivated “point-like” definition,

$$\begin{aligned} \frac{F_i}{F_p} - 1 &< \delta_F, \\ \left| \frac{\Theta_M}{\Theta_{\text{maj}}} - 1 \right| &< \delta_S, \\ \left| \frac{\Theta_m}{\Theta_{\text{min}}} - 1 \right| &< \delta_S, \end{aligned}$$

allowing small tolerances, which, by default, are 10% (i.e., $\delta_F = \delta_S = 0.1$).

We apply a near-field cutoff, excluding sources $> 0.3^\circ$ from the phase centre, corresponding to a (normalized) primary beam power of $\mathcal{A} > 75\%$. The exclusion of far-field sources minimizes the errors from direction-dependent effects. Lastly, we exclude highly variable and transient sources that would exhibit significant changes in their signal-to-noise ratios. Any sources with maximum and minimum peak intensities separated by a factor ≥ 2 or missing from $\geq 25\%$ of the epochs are removed from each catalogue. The astrometry routine proceeds as follows:

1. With PYBDSF, extract a catalogue of each observation, removing sources that fail the point-like conditions. The catalogues are cross-matched to one another, adopting a single observation as the reference.

Sources separated by less than $\Theta_{\text{maj}}/3$ are taken as matches. The final catalog consists of n_{obs} observations of n_{src} sources, such that each source j has a position $(\alpha_{i,j}, \delta_{i,j})$ and a signal-to-noise of $(S/N)_{i,j}$, in observation i .

2. Calculate the average position of each source (average over index j), weighting each observation using the size of the PSF along the RA/Dec directions (to the 68% confidence region); i.e., inverse-variance weightings, $\mathcal{D}_{\text{RA/Dec}}^{-2}$.
3. Bootstrap the positions to estimate the uncertainty on $(\hat{\sigma}_r)_j$. For each source, create n_{boot} bootstrapped samples of length n_{obs} , re-sampling (with replacement) the positions from each observation. Assuming the average value from (2) represents the true position of each source, calculate the dimensionless astrometric errors in each bootstrap sample.
4. For each source, adopt the median value from the bootstrapped samples as $(\hat{\sigma}_r)_j$, quantifying the $(-)/(+)$ 1σ uncertainties as the range between the median and the 16th/84th percentile. These uncertainties are symmetric, so adopt the average of the $(-)/(+)$ for the following MCMC fitting.
5. Calculate the median signal-to-noise ratio for each source, $(S/N)_j$.
6. Solve for the astrometric error parameters A and B . We solve for A and B with a similar MCMC approach as applied in Section 3.2.3. Assume $(\hat{\sigma}_r)_j$ values are independent and normally distributed, adopting flat uninformative priors for A and B , with the only constraint being that $A, B \geq 0$. These A and B values quantify the *uncorrected* astrometric error.
7. Solve for the per-observation average astrometric correction (average across index i) in RA and Dec. The averages are inverse-variance

weighted, using the parameters from (6) and Equation (6.8).

8. Correct the positions with the per-observation corrections and repeat steps (1)→(7) until convergence. The uncertainty on the per-observation correction is included in each subsequent bootstrap sample; add a random offset drawn from a normal distribution with a standard deviation fixed as the uncertainty in the per-observation correction.
9. We define a convergence parameter C between run n and $n + 1$ as,

$$C = \frac{|(\hat{\sigma}_{r,j})_{n+1} - (\hat{\sigma}_{r,j})_n|}{\sqrt{(\Delta\hat{\sigma}_{r,j})_{n+1}^2 + (\Delta\hat{\sigma}_{r,j})_n^2}}.$$

Defining convergence to occur after $C < 0.1$ for three consecutive iterations. The final values of A and B quantify the *corrected* astrometric error.

The routine, ASTKAT, is publicly available⁴ and allows the user to simulate images for code verification as well as modify the parameters that control cataloguing, filtering, bootstrapping, and convergence. We solve for $\mathcal{D}_{RA/Dec}$ by marginalizing the PSF along the RA/Dec directions using these values to estimate the errors on individual RA and Dec measurements.

‘

6.3 Results

The astrometric fit for our three XRB fields is presented in Fig. 6.3 through Fig. 6.5. Additionally, we tabulate the fit parameters in Table 6.1, including the reduced statistic χ_{red}^2 and a ‘fractional FWHM equivalent’ ($B \times \sqrt{s/8 \ln 2}$) to quantify the systematic astrometric limit as a fraction of the PSF FWHM.

⁴<https://github.com/AKHughes1994/AstKAT>